



Assessment of Mechanically Induced Changes in Helical Fiber Microstructure Using Diffusion Tensor Imaging

Roberto Alonso Pineda Guzman¹ · Noel Naughton² · Shreyan Majumdar² · Bruce Damon^{2,3,4,5,6,7,8} · Mariana E. Kersh^{1,2,8} 

Received: 19 July 2023 / Accepted: 4 December 2023
© The Author(s) under exclusive licence to Biomedical Engineering Society 2023

Abstract

Noninvasive methods to detect microstructural changes in collagen-based fibrous tissues are necessary to differentiate healthy from damaged tissues *in vivo* but are sparse. Diffusion Tensor Imaging (DTI) is a noninvasive imaging technique used to quantitatively infer tissue microstructure with previous work primarily focused in neuroimaging applications. Yet, it is still unclear how DTI metrics relate to fiber microstructure and function in musculoskeletal tissues such as ligament and tendon, in part because of the high heterogeneity inherent to such tissues. To address this limitation, we assessed the ability of DTI to detect microstructural changes caused by mechanical loading in tissue-mimicking helical fiber constructs of known structure. Using high-resolution optical and micro-computed tomography imaging, we found that static and fatigue loading resulted in decreased sample diameter and a re-alignment of the macro-scale fiber twist angle similar with the direction of loading. However, DTI and micro-computed tomography measurements suggest microstructural differences in the effect of static versus fatigue loading that were not apparent at the bulk level. Specifically, static load resulted in an increase in diffusion anisotropy and a decrease in radial diffusivity suggesting radially uniform fiber compaction. In contrast, fatigue loads resulted in increased diffusivity in all directions and a change in the alignment of the principal diffusion direction away from the constructs' main axis suggesting fiber compaction and microstructural disruptions in fiber architecture. These results provide quantitative evidence of the ability of DTI to detect mechanically induced changes in tissue microstructure that are not apparent at the bulk level, thus confirming its potential as a noninvasive measure of microstructure in helically architected collagen-based tissues, such as ligaments and tendons.

Keywords Fiber · Microstructure · Mechanics · Fatigue · Diffusion MRI

Introduction

Over one third of all musculoskeletal injuries in the United States involve connective tissue deterioration, resulting in an annual incidence of more than 10 million injuries [1]. To detect damage accumulation and improve the detection

Associate Editor Elizabeth Cosgriff-Hernandez oversaw the review of this article.

✉ Mariana E. Kersh
mkersh@illinois.edu

¹ Department of Mechanical Science & Engineering, University of Illinois Urbana-Champaign, Urbana, IL, USA

² Beckman Institute for Advanced Science & Technology, University of Illinois Urbana-Champaign, Urbana, IL, USA

³ Carle Clinical Imaging Research Program, Stephens Family Clinical Research Institute, Carle Health, Urbana, IL, USA

⁴ Department of Bioengineering, University of Illinois Urbana-Champaign, Urbana, IL, USA

⁵ Department of Biomedical Engineering, Vanderbilt University, Nashville, TN, USA

⁶ Vanderbilt University Institute of Imaging Science, Vanderbilt University Medical Center, Nashville, TN, USA

⁷ Department of Radiology and Radiological Science, Vanderbilt University, Nashville, TN, USA

⁸ Carle Illinois College of Medicine, University of Illinois Urbana-Champaign, Urbana, IL, USA

and treatment of connective tissue injuries, it is necessary to quantify the underlying determinants that differentiate healthy from damaged soft tissues. Damage accumulation from repetitive loading manifests as changes in tissue microstructure [2]; however, most methods used to quantify connective soft tissue microstructure involve microscopic imaging [2–5] which requires excision of tissue for examination.

Diffusion Tensor Imaging (DTI) is a noninvasive Magnetic Resonance Imaging (MRI) technique that measures the diffusion properties of water in tissues [6]. DTI is sensitive to physical barriers that restrict the movement of water molecules, providing a proxy measure of tissue microstructure. For example, the DTI metric radial diffusivity (RD) measures the degree to which water molecules are free to move in the direction perpendicular to the principal orientation of physical barriers in a material. Assuming the physical barriers mediating diffusion are transversely isotropic, RD provides an indicator of the compaction of the physical barriers (e.g. collagen fibers, cells, or other constituents of the tissue) that would impede diffusion: tightly packed aligned fibers result in low RD and high axial diffusivity (AD). DTI metrics have been used to research brain neuronal structure [7], and in smaller scope, skeletal muscle [8–10]. Efforts to study connective collagen-rich tissues (breast, cartilage, artery, and cervix) are sparse, but have related DTI metrics to microstructure [11–16], and biomechanical function [17].

DTI has been used to quantitatively assess pathologies and clinical interventions in ligaments and tendons [18–26]. However, these studies are limited to correlations between DTI metrics and injury states and lack information on the biomechanical causation of these relationships. To our knowledge, only one study has related DTI metrics to tissue composition in tendon [27] but did not relate DTI metrics to microstructural assessments. A clear understanding of the relationship between collagen fiber microstructure, mechanical behavior, and DTI metrics is needed but is challenging because of the heterogeneous nature of ligaments and tendons [28] and the multifactorial contribution of cellular and non-collagenous extracellular components to the DTI metrics measured in biological materials [29].

To circumvent these challenges, tissue-mimicking materials with known fiber architecture can be used as microstructural phantoms and provide a platform to probe the sensitivity of DTI measurements to detect changes in fiber microstructure [30]. Anisotropic fiber phantoms have been used to model brain white matter, demonstrating that diffusion anisotropy increases with increased fiber density [31, 32] and that principal diffusion direction follows the principal orientation of the tissue fiber structure [33, 34]. In silico models of articular cartilage fiber networks have been used to study the effect of fiber density, orientation, and organization on diffusion properties [35]. However, hierarchical,

helical fiber structures, such as those found in ligament and tendon [36, 37], have yet to be assessed with DTI.

Similar to ligament and tendon, engineered helical fiber constructs transfer loads through interfibrillar shear between discontinuous fibers [38–40], and lose volume in response to uniaxial tensile loading [41, 42]. Previously, we demonstrated that helically architected fiber constructs mimic the hierarchical microstructure and tensile behavior of ligaments [43]. These fiber constructs have also been used to replicate the shear behavior of tendon and ligament [44]. Additionally, the constructs' fiber diameters (10–20 μm) and fiber separation distances (10–40 μm) are at the same length scale of collagen fibers in tendon and ligament [45]. This ability to mimic the fiber microstructure and ex vivo mechanics of ligament and tendon makes helically architected fiber constructs an ideal microstructural DTI phantom for these tissues.

Using tissue-mimicking fiber constructs as microstructural DTI phantoms, the aim of this study was to establish relationships between fiber microstructure, mechanical function and DTI metrics. We quantified the changes in structure and DTI metrics caused by mechanical loading on the tissue-mimicking fibers. These relationships will provide the necessary framework for future studies to interpret mechanically induced changes in DTI metrics in biological ligaments, tendons, and other transversely isotropic and helically architected collagen-based tissues.

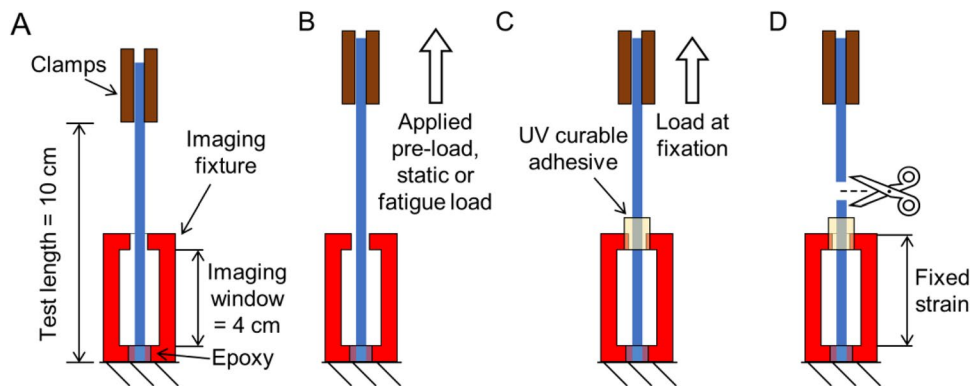
Materials and Methods

Fifteen helically architected tissue-mimicking samples (Caron, linear density = 590 tex, Listowel, ON, Canada) [43] were used in this study. The samples were randomly assigned to three groups ($n = 5/\text{group}$): control, static load, and fatigue load. After undergoing their respective loading protocol, the samples were fixed at their final loaded configuration. High resolution images were obtained to characterize the bulk structure of all the samples and microCT scans were obtained in one sample of each group to characterize fiber microstructure. DTI scans were obtained on all the samples while submerged in water, with the goal of identifying DTI metrics that can characterize mechanically induced microstructural changes between the sample groups.

Sample Preparation

A custom MRI compatible fixture, with a 4 cm optical imaging window, was used to secure and image the samples after mechanical loading (Fig. 1A). One end of the sample was attached to the fixture using water-resistant epoxy (J-B MarineWeld, Marietta, GA, USA). The free end of the samples was clamped to mechanically load the

Fig. 1 Schematic showing the preparation and mechanical loading procedure of the tissue-mimicking samples. The procedure consisted of **A** mounting of samples for mechanical loading, **B** loading protocol, **C** fixation of the sample at the end of loading, **D** detachment of sample from external load while preserving sample strain



samples (Fig. 1B). After the final load was reached, the samples were fixed to the MRI compatible fixture using an ultraviolet (UV) curable adhesive (Blufixx PW, Weseling, Nordrhein-Westfalen, Germany) (Fig. 1C). The strain in the sample was preserved within the imaging fixture by the fixation and the sample was cut outside of the imaging fixture to remove the external applied loads (Fig. 1D). Finally, the samples were imaged at their final loaded configuration.

Mechanical Loading Protocols

An exposed test length of 10 cm was used for all samples. The samples were subjected to 50 preconditioning axial loading cycles (2–25 N, 1.15 Hz) prior to mechanical loading.

Unloaded controls: The control group was loaded to 0.2 N using a uniaxial testing system (Instron model 5967, Instron, USA) to standardize the initial length of the samples and then fixed in place. The samples were then attached to the fixture using the UV curable adhesive.

Static Load: The free end of the static sample group was clamped using pneumatic grips. The samples were loaded to 5 N and then attached to the fixture using the UV curable adhesive. Static loading data were collected at 100 Hz.

Fatigue Load: The samples assigned to the fatigue group were subjected to 10,000 loading cycles using a uniaxial dynamic mechanical system (ElectroForce 3200, TA Instruments, New Castle, DE, USA) using a sinusoidal waveform ramping between 2–25 N at 5 Hz. Ten loading cycles were needed for the dynamic testing system to achieve a steady state of the 2–25 N load limits. Displacement data were collected for all samples at the 2 and 25 N load points for each loading cycle and continuous mechanical data were collected for one sample at 500 Hz. Following fatigue loading, the samples were loaded to 0.2 N and then secured within the imaging fixture.

The maximum strain, $\epsilon_{max,n}$, during each fatigue cycle (n) was computed as:

$$\epsilon_{max,n} = \frac{u_{25N,n} - u_{2N,10}}{100 \text{ mm}} \times 100\% \quad (1)$$

where $u_{25N,n}$ was the displacement at 25 N for cycle n , $u_{2N,10}$ was the displacement at 2 N for the 10th cycle, and 100 mm was the original length of the sample.

The cyclic stiffness was computed as:

$$k_n = \frac{25N - 2N}{u_{25N,n} - u_{2N,n}} \quad (2)$$

where $u_{25N,n}$ and $u_{2N,10}$ were the displacement at 25 N and 2 N for cycle n , respectively. The difference between the maximum and minimum cyclic load was assumed to be 23 N per the fatigue protocol. All analyses were performed in MATLAB (version R2018b, Mathworks, Natick, MA, USA).

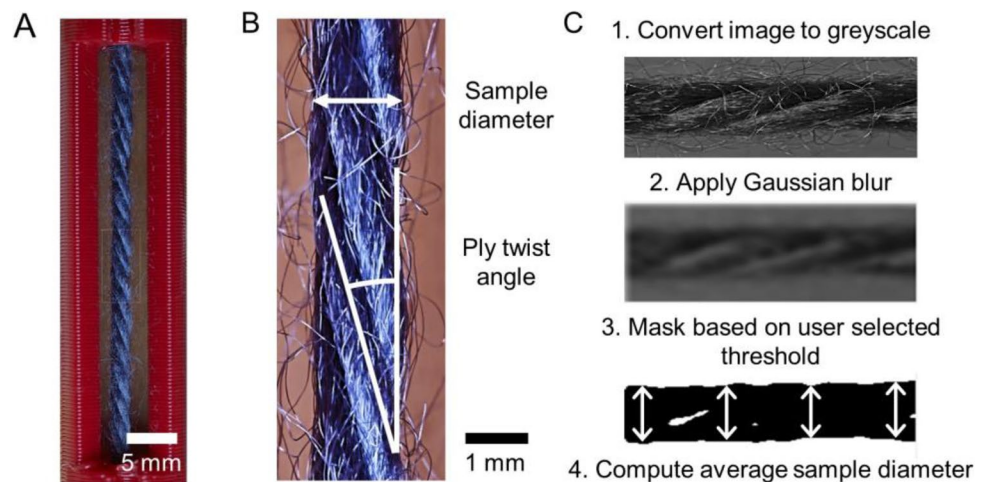
Bulk Scale Structural Imaging

All samples were imaged within the fixture's imaging window (Fig. 2A) using a high-resolution camera (PhaseOne XF IQ3 100 MP, Copenhagen, Denmark) to measure the sample diameter and ply twist angle (Fig. 2B, C), indices of the primary hierarchical structure, using custom MATLAB code (version R2018b, Mathworks, Natick, MA, USA) and ImageJ (National Institutes of Health, Bethesda, MD, USA). Sample diameter was measured by segmenting the sample from the background, binarizing the image, and calculating the mean distance between the sample edges. The ply twist angle of each sample was measured manually using ImageJ (Fig. 2B).

Microstructural Imaging

Micro-Computed Tomography (microCT) scans of one sample from each group were acquired to quantify ground truth fiber microstructure. The control and static load samples were scanned using an Xradia MicroXCT 400 (Zeiss, Oberkochen, Baden-Württemberg, Germany) scanner (voltage = 25 kV, power = 5 W, resolution = $2.1 \times 2.1 \times 2.1 \mu\text{m}$, field of view = $2.08 \times 2.08 \times 2.08 \text{ mm}$), while the fatigue

Fig. 2 **A** Image of fixed sample inside the imaging window. **B** Structural parameters measured on phantoms: phantom diameter and ply twist angle. **C** Procedure followed to measure phantom diameter from the high-resolution images



sample was scanned using a Rigaku CT Lab HX130 (Rigaku, Tokyo, Japan) scanner (voltage = 50 kV, source power = 8 W, resolution = $2.5 \times 2.5 \times 2.5 \mu\text{m}$, field of view = $2.36 \times 2.12 \times 2.47 \text{ mm}$). The fatigue sample was resized to have an in-plane resolution of $2.1 \times 2.1 \mu\text{m}$.

The microCT data were binarized (Amira, Thermo Fisher Scientific, Waltham, MA, USA) and imported into MATLAB (version R2018b, Mathworks, Natick, MA, USA). For each CT slice, the fiber density was quantified as the ratio between the total fiber pixel area and the area of the smallest polygon enclosing all the fibers. The second moment of area of the sample's fiber cross section with respect to the cross section's minor axis was computed to evaluate fiber dispersion.

Diffusion Tensor Imaging

Finally, DTI data were collected on all samples. The diffusion encoding parameters used for the DTI sequences were optimized through numerical simulations of the Bloch-Torrey equation [46] using a binarized cross-section of the sample's fibers that were acquired in a previous study using microCT [43]. A parameter sweep of gradient strengths and diffusion times was performed to identify the parameter combinations that would maximize the encoding of structural information into the diffusion-weighted signal, under the constraint of adequate signal-to-noise ratio (SNR).

The samples were submerged in distilled water and a vacuum chamber was used to remove air bubbles. The submerged samples were then imaged in a 9.4 T MRI system (Bruker, Billerica, MA, USA) using a circularly polarized volume coil with an outer/inner diameter of 112/86 mm for transmission, and a ^1H receive-only 2×2 rat brain array coil for reception. DTI was performed using an echo-planar imaging sequence (TE/TR = 180/4200 ms, 12 directions,

12 excitations, $b = 600 \text{ s/mm}^2$, diffusion gradient duration $\delta = 80 \text{ ms}$, and diffusion gradient separation $\Delta = 86 \text{ ms}$). Twenty slices were acquired per sample (slice thickness = $375 \mu\text{m}$, in-plane resolution = $150 \times 150 \mu\text{m}$, field of view = $19.2 \times 19.2 \times 7.5 \text{ mm}$). T2-weighted images were also acquired to visualize the sample geometry using a Rapid Imaging with Refocused Echoes (RARE) sequence (TE/TR = 10/4300 ms, slice thickness = $375 \mu\text{m}$, in-plane resolution = $150 \times 150 \mu\text{m}$, field of view = $19.2 \times 19.2 \times 7.5 \text{ mm}$). The T2-weighted images were used to segment the sample's region of interest (ROI) from the surrounding water by segmenting all voxels with at least a 15% decrease in the fibers T2-weighted signal relative to the signal measured in voxels corresponding to water.

All volumes acquired from the T2 and DTI scans were manually registered. SNR maps of the DTI images were computed using the *dwidnoise* function available in MRtrix3.0 [47, 48] and corrected using Koay's inversion technique [49]. The median, median absolute deviation, and range of the computed SNR was 22.4 ± 3.4 (15.4–38.6) in the control samples, 24.9 ± 1.9 (14.8–34.9) in the static load samples, and 25.2 ± 3.8 (12.5–38.1) in the fatigue samples. A voxel-based analysis with this level of SNR is inappropriate for anisotropic structures [50, 51]. To reduce the bias caused by noise when computing the diffusion tensor, the individual diffusion directional signals in the sample's ROI were averaged in each slice of the DTI scans. This signal averaging strategy effectively reduces the effect of noise in the DTI metrics of anisotropic structures with an average SNR > 20 in the non-diffusion weighted images [50]. Additionally, we ran a sensitivity study to determine that our signal averaging method is feasible at low SNR, see Supplementary document 1. The diffusion tensor of each slice was computed using the average non-diffusion weighted and diffusion weighted signals of each slice with the *signal2tensor2*

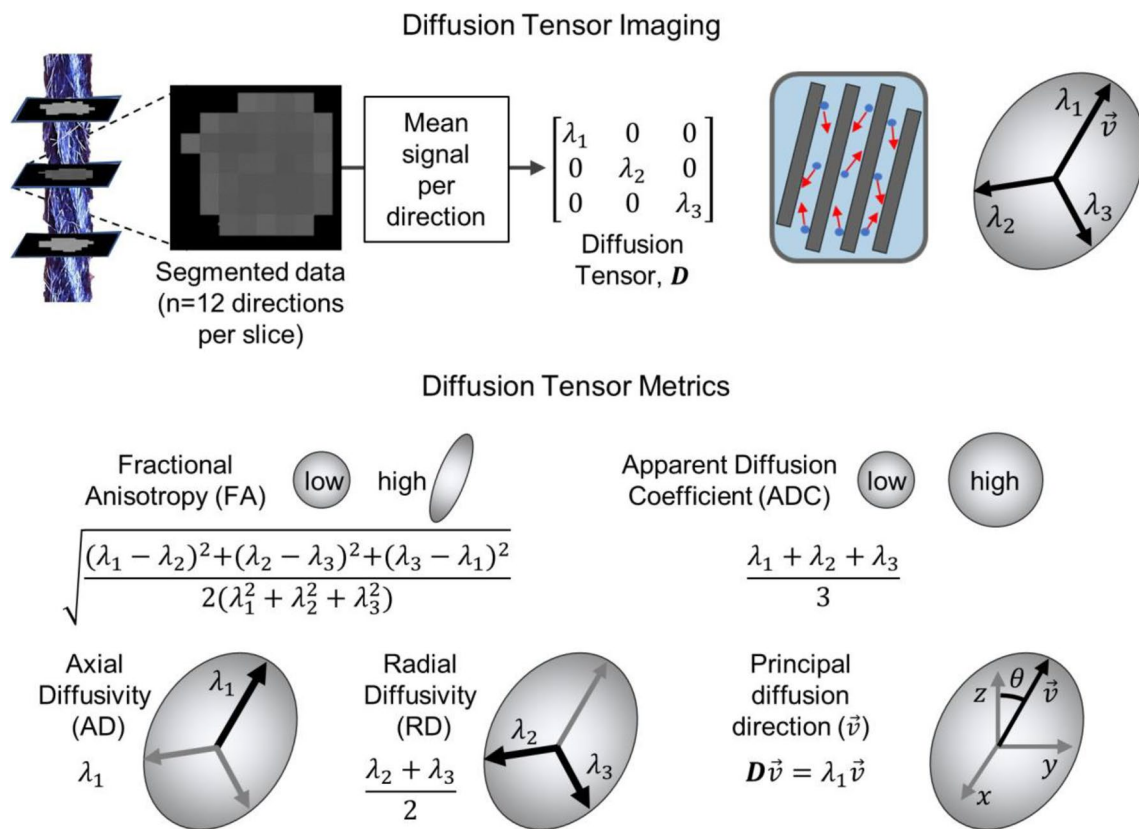


Fig. 3 Diffusion Tensor Imaging data obtained from phantoms submerged in distilled water and DTI metrics used to analyze the changes in fiber microstructure caused by the mechanical loading protocols

function of the publicly available DTI muscle toolbox [52] (Fig. 3). The tensor was diagonalized to calculate the principal eigenvalues (λ_1 , λ_2 , and λ_3). The eigenvalues were used to calculate the following DTI metrics:

Fractional anisotropy (FA) was calculated as:

$$FA = \sqrt{\frac{(\lambda_1 - \lambda_2)^2 + (\lambda_2 - \lambda_3)^2 + (\lambda_3 - \lambda_1)^2}{2(\lambda_1^2 + \lambda_2^2 + \lambda_3^2)}} \quad (3)$$

Apparent diffusion coefficient (ADC) was calculated as:

$$ADC = \frac{\lambda_1 + \lambda_2 + \lambda_3}{3} \quad (4)$$

RD was calculated as the mean of the 2nd and 3rd eigenvalues. AD is equivalent to the first eigenvalue and the principal diffusion direction (\vec{v}) indicates the direction of maximum diffusion (λ_1) calculated from the diffusion tensor \mathbf{D} . The Z-orientation angle, θ , between the sample's main axis and the principal diffusion direction was also computed. A structural interpretation of each MRI metric is shown in Fig. 3. All MRI data-processing steps, except for the noise computations, were conducted in MATLAB (version R2018b, Mathworks, Natick, MA, USA).

Statistical Analysis

Normality of all measurements was tested using a Shapiro-Wilks test. All structural property measurements were normally distributed, thus unpaired t-tests were used to evaluate the differences in the structural parameters between the sample groups ($\alpha = 0.05$). Differences between the distributions of microstructural parameters and DTI metrics of the static load and fatigued group with respect to the control group were evaluated using Kolmogorov-Smirnov tests ($\alpha = 0.05$). All statistical analyses were conducted in R (version 4.2.3).

Results

Effect of Loading on Mechanical and Structural Properties

Static Loading

Static loading resulted in a J-shaped load-strain curve reflecting a bulk scale mechanical response characteristic

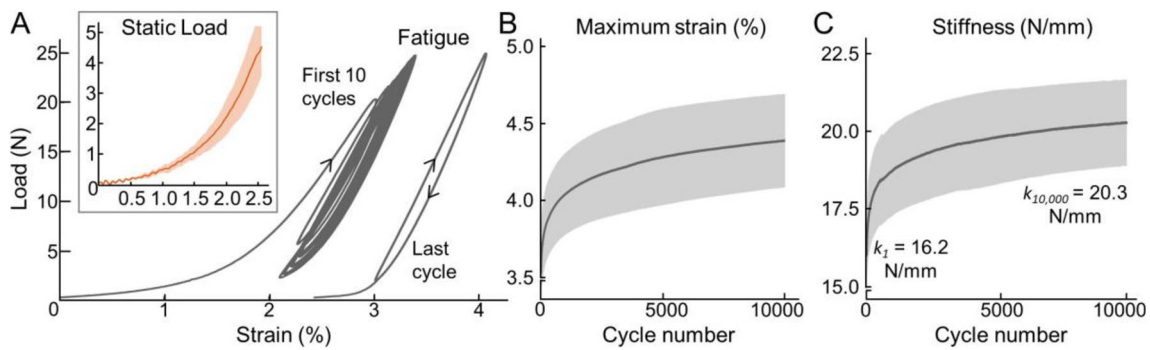


Fig. 4 Load–strain curves obtained from the static load (inset) and fatigue samples (A). Maximum strain (B) and stiffness (C) as a function of loading cycle on the fatigued samples

of collagen-rich tissues (Fig. 4A) [43, 53]. To reach the 5 N load, the samples were displaced 2.69 ± 0.23 mm ($2.69 \pm 0.23\%$ uniaxial strain). Static loading resulted in a 25.1% decrease in sample diameter from 1.79 ± 0.12 mm in the control samples to 1.34 ± 0.03 mm in the loaded samples

(Fig. 5A, $p < 0.001$). When compared to the control samples, the macroscopic ply twist angle decreased by 34.3% when subjected to static load, from a ply twist angle of $16.3 \pm 2.04^\circ$ in the control group to a ply twist angle of $10.7 \pm 0.63^\circ$ in the loaded group (Fig. 5B, $p = 0.002$).

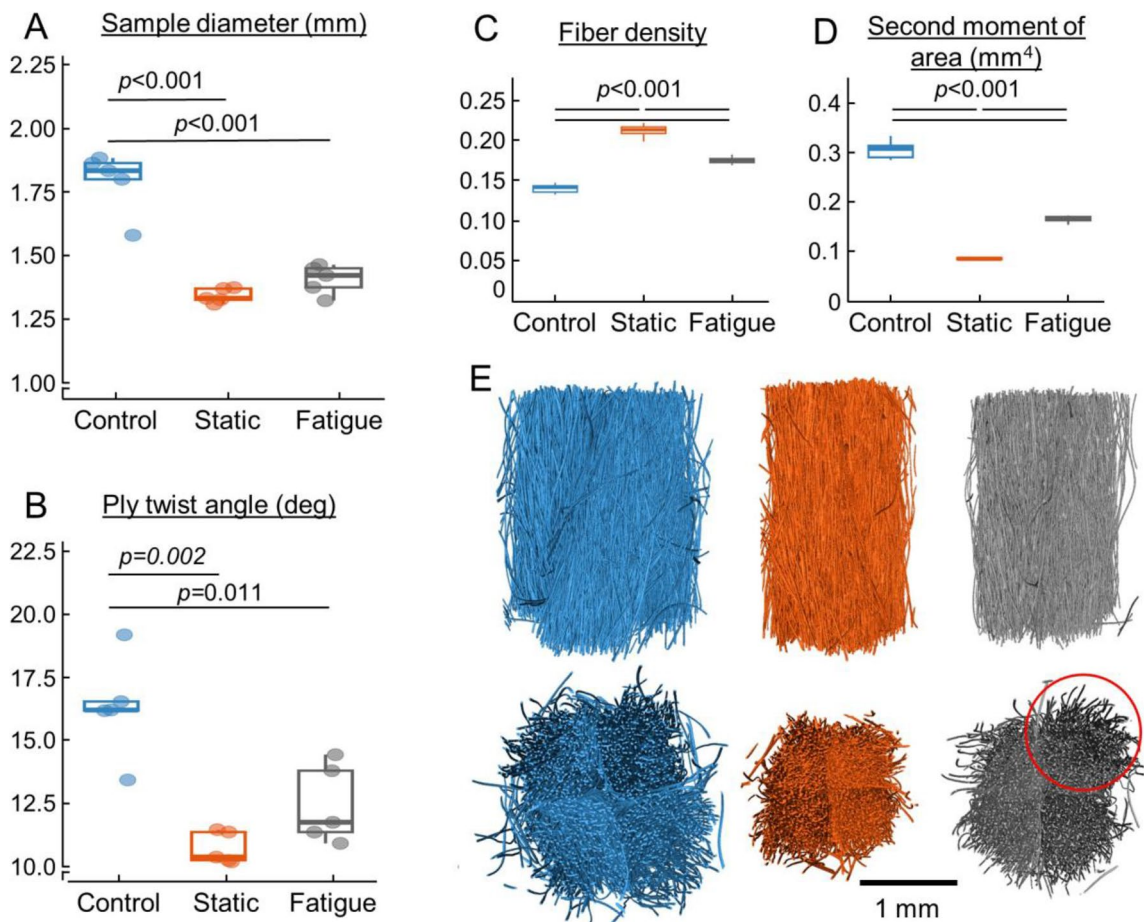


Fig. 5 Sample diameter (A) and ply twist angle (B) of the control, static load, and fatigue sample groups. Microstructural changes in fiber density (C) and second moment of area of the sample's cross

section (D) between groups. Micro-CT scan renderings of one sample of each group (E). The red circle highlights the observed fiber disruptions in the fatigued sample

The microCT analyses revealed changes in sample microstructure. The fiber density was initially 0.14 ± 0.003 for the control sample and increased by 50% ($p < 0.001$) to 0.21 ± 0.004 when subjected to static loading (Fig. 5C). The second moment of area was $0.307 \pm 0.011 \text{ mm}^4$ for the control sample and decreased ($p < 0.001$) to $0.08 \pm 0.0012 \text{ mm}^4$ under static load (Fig. 5D), $p < 0.001$).

Fatigue Loading

Similar to the static load case, the fatigue loading protocol resulted in a J-shaped load-strain response. All samples reached the secondary phase of fatigue loading by 10,000 loading cycles, which is characterized by a steady increase in the maximum strain and stiffness followed by the rapid increase observed in the primary phase [54] (Fig. 4A–C). Fatigue loading resulted in a $24.5 \pm 4\%$ increase in max cyclic displacement and a $24.1 \pm 0.7\%$ increase in cyclic stiffness.

The fatigue loading protocol resulted in measurable macrostructural changes compared to unloaded samples and were similar to the changes that occurred due to static loading. Fatigue loading decreased the sample diameter by 21.9% when compared to the control group ($p < 0.001$, Fig. 5A). The mean ply twist angle of the fatigued group decreased by 23.7% ($p = 0.011$) with respect to the control group (Fig. 5B).

Fatigue loading resulted in a 23.7% increase in median fiber density (0.174 ± 0.003 for fatigue, Fig. 5C). The median second moment of area decreased to $0.165 \pm 0.003 \text{ mm}^4$ following fatigue loading ($p < 0.001$, Fig. 5D). Notably, we observed local regions of fiber disruption in the microCT data of fatigued samples that were not observed with static loading (Fig. 5E).

Effect of Loading on DTI Metrics

Of the DTI metric data, the FA, ADC, and RD of the control samples, the ADC of the static load samples, and the RD of the fatigue samples were normally distributed. The remaining data sets were non-normally distributed. Thus, we describe the results of DTI measurements using medians and median absolute deviations.

Tensile static loading resulted in changes in FA and RD. FA increased by 28.1% ($p < 0.001$), from 0.32 ± 0.04 in the control group to 0.41 ± 0.05 in the loaded group. RD decreased by 13.0% ($p < 0.001$) with static loading when compared to the control group, from $0.81 \pm 0.10 \times 10^{-3}$ to $0.70 \pm 0.10 \times 10^{-3} \text{ mm}^2/\text{s}$. Static loading did not significantly change ADC, AD, and Z-orientation angle compared to the control samples (Fig. 6).

Fatigue loading resulted in changes to the ADC, AD, RD, and the Z-orientation angle of the principal diffusion direction (θ). ADC increased 5.85% to $1.06 \pm 0.13 \times 10^{-3} \text{ mm}^2/\text{s}$ ($p = 0.003$), median AD increased 8.2% to $1.47 \pm 0.16 \times 10^{-3} \text{ mm}^2/\text{s}$ ($p < 0.001$), and median RD increased 4.94% to $0.85 \pm 0.11 \times 10^{-3} \text{ mm}^2/\text{s}$ ($p = 0.024$). The Z-orientation angle of the fatigued samples increased by 31.1% ($p = 0.024$) compared to the control samples, with a Z-orientation angle of $5.82 \pm 2.80^\circ$ in the fatigued samples compared to $4.44 \pm 1.6^\circ$ in the control samples (Fig. 6). These fatigue-induced changes were not homogeneous along the length of the sample; but instead were observed in specific locations along the samples' length (Fig. 6E), which are coincident with fiber disruptions observed in the microCT data of the same sample but not apparent at the bulk level (Fig. 7).

Discussion

This study identified DTI metrics related to mechanically induced changes in tissue-mimicking phantoms. In the samples loaded under static tension, we found that increasing FA and decreasing RD were related to fiber compaction and increased fiber density (Fig. 8). Previous studies have shown that FA is directly proportional to the fiber density of parallel fiber phantoms [31, 33]. While no data, to our knowledge, is available on how ADC, RD, and AD change as a function of fiber density in physical phantoms, in silico modeling of water diffusion in fiber networks shows that RD is more likely to be affected by an increase in fiber density than AD [35].

The decrease in sample diameter and ply twist angle and increase in fiber density of the static load group agrees with a mathematical formulation that accounts for fiber diametrical compaction as the main microstructural mechanism driving the sample's low-stress tensile behavior [42]. This formulation takes into account the compressibility of fiber-based materials derived from van Wyk's theory [55] and assumes negligible fiber sliding, interfibrillar friction, and fiber stretch during the toe region of the sample's load–displacement curve. Our results support the role of fiber diametrical compaction as a potential mechanism that can explain the toe region and large Poisson's ratio [56] observed in ligaments and tendons with helically architected collagen fibrils and fibers. Coupled with the shear lag models [39], a more comprehensive microstructural description can be provided for the tensile behavior of ligaments and tendons.

In the fatigued samples, we found an increase in ADC, AD, and RD that suggests an increase in fiber disorganization, as more disorganized fiber structures would allow for more water diffusion. Increases in fiber disorganization could also account for the changes in principal diffusion

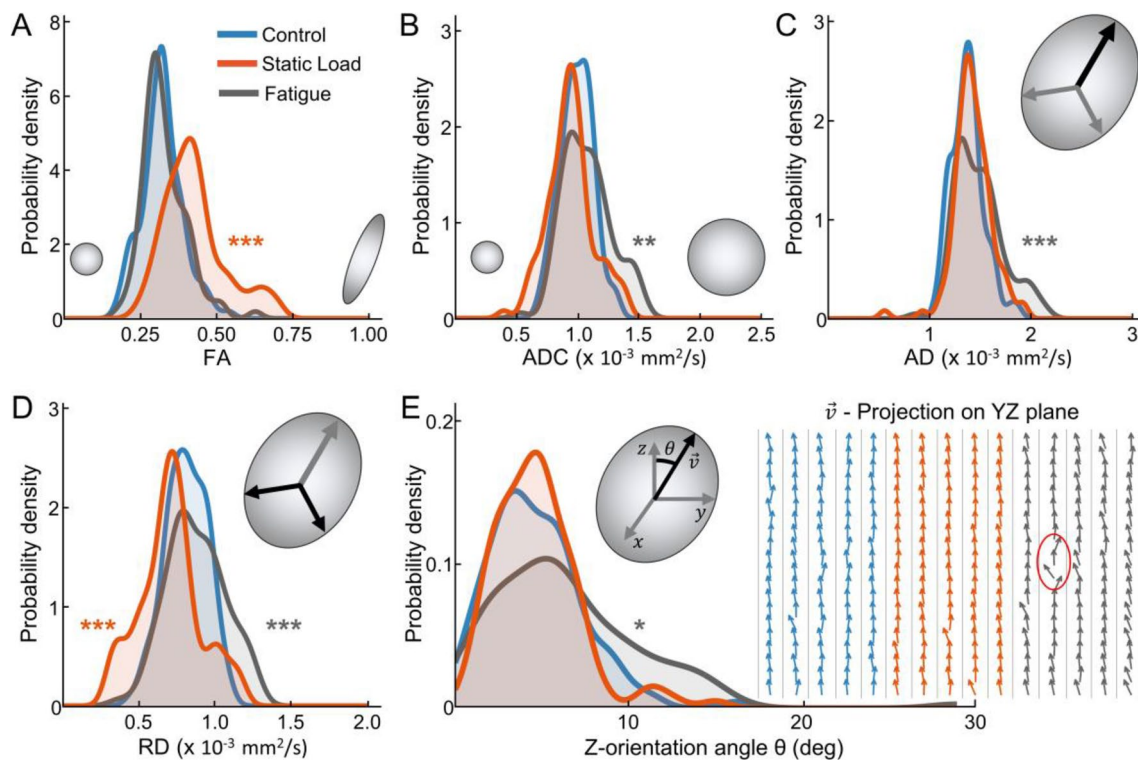


Fig. 6 A–D Probability density distributions of FA, ADC, AD and RD in the control, static load, and fatigue groups. **E** Probability density distribution of the Z-orientation angle in the three groups and visualized projection of the principal diffusion direction (\vec{v}). Each arrow represents the YZ projection of \vec{v} computed on each slice and

each column represents the twenty slices of each sample. Arrows circled in red highlight a local misalignment in \vec{v} . * $p < 0.05$; ** $p < 0.01$ and *** $p < 0.001$ refer to comparisons with respect to the control group

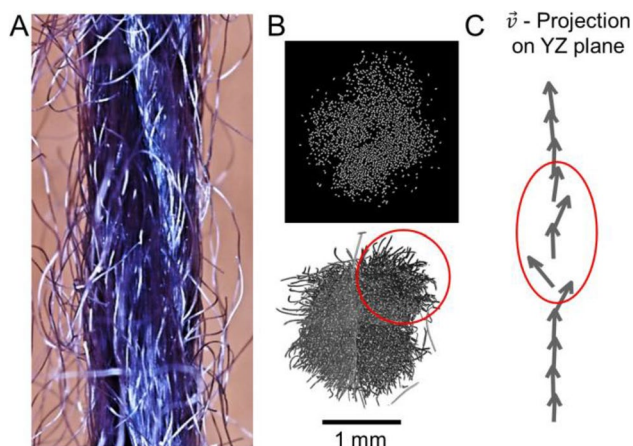


Fig. 7 High resolution image (A), microCT rendering (B), and YZ projections of the principal diffusion direction, \vec{v} , (C) in the central area of the imaging window of one of the samples in the fatigue group

direction and Z-orientation angle measured in the fatigued samples as disrupted fiber architecture could allow for more diffusion along the radial direction of the sample (Fig. 8).

Our microstructural data suggests that fatigued samples have local disruptions in fiber microstructure that account for these changes in DTI metrics (Fig. 6E). The principal diffusion direction has been used as a surrogate for fiber orientation in both composite and biological fiber-based materials [11, 14, 57], thus our results suggest that fatigue loading results in microstructural disruptions that create axial misalignments in fiber microstructure.

Fatigued samples resulted in a biphasic fatigue behavior (Fig. 4A–C) similar to tendons [58, 59] and fiber-based composites [60]. Although the microstructural mechanisms driving this behavior remain unknown, the fiber architecture of both tendon and fiber-based composites show a disruption in fiber architecture during the second phase of fatigue loading [2, 58–60]. Our results agree with these studies, as the DTI metrics and microCT data indicate a disruption in the fiber architecture in the fatigued group. Thus, DTI metrics may provide further insight into the microstructural changes in tissues that occur as a result of different pathologies.

In a previous study in the Achilles tendon, higher FA was correlated to lower collagen content and lower collagen alignment while higher ADC, AD, and RD were correlated to higher collagen content [27]. In breast cancer

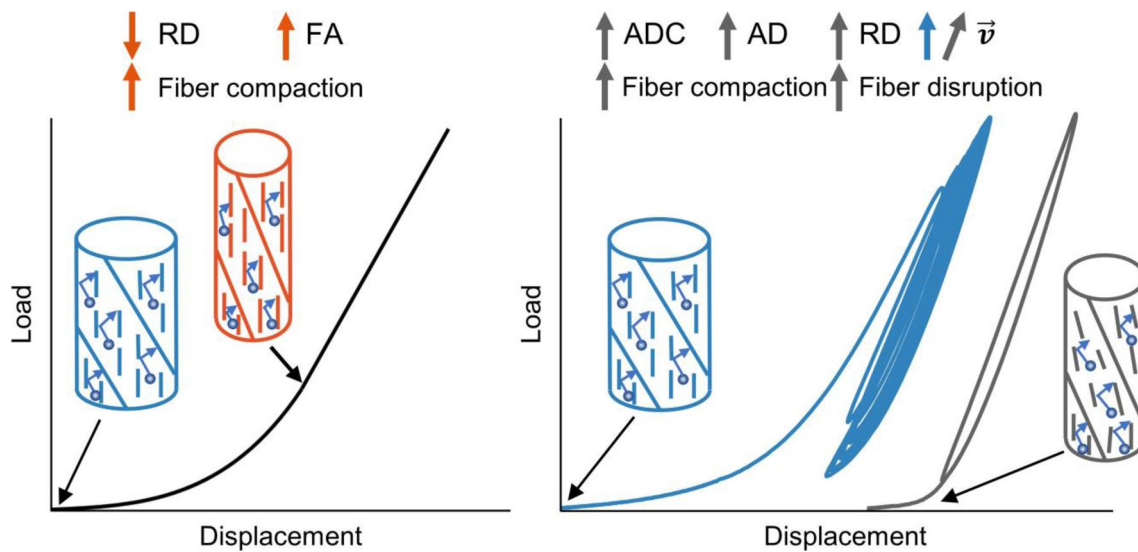


Fig. 8 Schematic showing the changes in structure and DTI metrics caused by tensile and fatigue loading in tissue-mimicking phantoms

tissue, higher ADC was correlated to higher collagen content but FA was inversely correlated [11]. Thus, it is not clear whether tissue specific interpretations of DTI metrics and their relationship to the tissue microenvironment are required to explain these contrasting findings with respect to FA. Nonetheless, DTI metrics have been correlated to clinical level findings.

In vivo studies of injured knee Anterior Cruciate Ligaments (ACLs) found a decrease in FA in those with higher levels of injury [23]. Anterior knee laxity is related to the mechanical integrity of the ACL [61] such that increased laxity (or ligament slack) in an injured knee indicates either structural or compositional degradation. After internal bracing, FA in the ACL has been reported to decrease and was hypothesized to be caused by an altered geometrical configuration of the tissue and was inversely correlated to knee laxity [22]. This is consistent with our results, as the application of tensile loading to remove the slack from our samples significantly increased their FA. Because the organization of cells in ligaments and tendons follows reorganization of collagen fibers due to their slackness [62], collagen fiber architecture could be an appropriate mediator of DTI metrics in this scenario. Both cellular and non-collagen extracellular components may also play a role in the DTI metrics of collagen-based tissues [29] and therefore a combination of both collagen fiber architecture and cellular content could explain these results. Notably, in the case of injury, swelling and inflammation may also contribute to changes in diffusion metrics.

Because our future goal is to assess the ability of DTI to measure the collagen fiber microstructure of tendons and ligaments and quantify mechanically induced changes in these tissues, our phantoms provide a platform that allows

us to only take into account changes in fiber architecture and confirm the sensitivity of DTI metrics to changes in fiber microstructure. Previously, in silico and fiber based phantoms have been used to assess changes in cartilage [35] and white matter [31–33]. Since our phantoms are reproducible, have a tissue-mimicking well characterized microstructure, and induce diffusion-related changes, they are suitable for use as DTI phantoms [30] of helically architected fibers. To the best of our knowledge, this type of fiber architecture has not been studied before using DTI. More importantly, the loading modes addressed in this study are relevant in ligaments and tendons, as these tissues are primarily loaded uniaxially along the primary orientation of their collagen fibers [63]. Static loads are exerted in these tissues during quiet standing to maintain adequate posture, while repeated loading cycles are experienced in elite sports and intensive manual labor. The effect of these loading modes in the collagen fiber microstructure of ligaments and tendons has been previously studied using invasive imaging techniques [2, 5, 58, 64], and changes along the length of ligaments and tendons have been observed as a result of repeated mechanical loading [2, 65]. Hence, our results are an important step to identify the ability of DTI to noninvasively detect mechanically induced changes along the length of these tissues.

A limitation to this study is that we were not able to analyze the DTI metrics of our phantoms at the in-plane resolution in which the data was acquired. Because the phantoms are made of acrylic, the volume occupied by the phantom's fibers is MRI-invisible and decreases the overall signal acquired in each voxel. This led to some local areas of the samples having low SNR that could confound the DTI metrics we measured. This problem was solved by averaging the signals within the

sample cross-section[50], at the expense of in-plane resolution. This method is conservative in nature such that our identification of disrupted areas is likely reflective of larger changes in microstructure at the voxel level. However, the variation along the samples' length was still quantified and differences were observed between the different sample groups, establishing the ability of DTI to detect differences between the fiber microstructure of the sample groups. Another limitation is that our microstructural measurements were limited to one sample per group and are not co-registered to the DTI data we measured. We believe, nevertheless, that our microCT data are representative of the microstructural changes caused by mechanical loading in the three groups of samples. The frequency and extent of fiber disruptions that occurred due to fatigue, as well as the mechanisms that caused these disruptions, could be assessed in future studies.

Finally, the validity of these results in the complex environment of tendons, ligaments, and other biological tissues needs to be confirmed and is the subject of future work. We believe, however, that our results provide a framework to evaluate how DTI metrics are affected by changes to collagen fiber microstructure in ligaments and tendons. The ability of DTI to noninvasively detect microstructural changes within a macroscopic field of view support the use of DTI to noninvasively assess microstructural disruptions in biological and composite materials. Since current microscopic assessments in biological and composite materials are invasive and highly localized, DTI could become an important tool to conduct damage analysis in fiber-based materials and more importantly ligaments, tendons, and other musculoskeletal soft tissues [66]. Additionally, there is an opportunity to explore more localized changes in fiber architecture via DTI tractography. Thus, DTI metrics may serve as a biomarker for microstructural changes indicative of mechanical function of ligaments, tendons, and other collagen-rich tissues and could detect damage prior to failure and monitor clinical interventions of ligaments and tendons in the clinical setting.

Conclusion

This work describes the ability of DTI to detect mechanically induced changes in a tissue-mimicking microstructural phantom. We show that tensile loading results in increased fiber density caused by the diametrical compression of helically architected fibers and is associated with higher FA and lower RD. We also show that fatigue loading results in fiber architecture disruption that result in higher ADC, AD, and RD as well as a disruption in the alignment of the principal diffusion direction with the phantom's main axis. These results provide a framework to assess the ability of DTI to detect mechanically induced changes in the collagen fiber

microstructure of ligaments, tendons and other helically architected collagen-based soft tissues.

Supplementary Information The online version contains supplementary material available at <https://doi.org/10.1007/s10439-023-03420-w>.

Acknowledgements This project was funded by the Jump ARCHES endowment through the Health Care Engineering Systems Center and with support from the Biomedical Imaging Center of the Beckman Institute for Advanced Science and Technology at the University of Illinois Urbana-Champaign (UIUC-BI-BIC). We would like to acknowledge Tanya Josek and Josh Gibson from the Microscopy Suite of the Beckman Institute for obtaining the microCT images of the samples, Travis Ross from the Visualization Laboratory of the Beckman Institute for his technical assistance with the high-resolution camera systems, and David Ehrhardt from the Advanced Materials Testing and Evaluation Lab at the University of Illinois for the equipment and technical assistance needed to conduct the fatigue testing of the samples. Helpful discussions with Professor Brad Sutton are also gratefully acknowledged. This work was supported by NIH/NIAMS grant R01 AR073831 to Bruce Damon.

Declarations

Conflict of interest None.

References

1. United States Bone and Joint Initiative, The Burden of Musculoskeletal Diseases in the United States (BMUS), 2014. <http://www.boneandjointburden.org>
2. Szczesny, S. E., C. Aeppli, A. David, and R. L. Mauck. Fatigue loading of tendon results in collagen kinking and denaturation but does not change local tissue mechanics. *J. Biomech.* 71:251–256, 2018. <https://doi.org/10.1016/j.jbiomech.2018.02.014>.
3. Chen, J., J. Kim, W. Shao, S. H. Schlecht, S. Y. Baek, A. K. Jones, T. Ahn, J. A. Ashton-Miller, M. M. Banaszak Holl, and E. M. Wojtys. An Anterior cruciate ligament failure mechanism. *Am. J. Sports Med.* 47(9):2067–2076, 2019. <https://doi.org/10.1177/0363546519854450>.
4. Kim, J., S. Y. Baek, S. H. Schlecht, M. L. Beaulieu, L. Bus-sau, J. Chen, J. A. Ashton-Miller, E. M. Wojtys, and M. M. Banaszak Holl. Anterior cruciate ligament microfatigue damage detected by collagen autofluorescence in situ. *Journal of Experimental Orthopaedics.* 9(1):74, 2022. <https://doi.org/10.1186/s40634-022-00507-6>.
5. Skelley, N. W., R. M. Castile, T. E. York, V. Gruev, S. P. Lake, and R. H. Brophy. Differences in the microstructural properties of the anteromedial and posterolateral bundles of the anterior cruciate ligament. *Am. J. Sports Med.* 43(4):928–936, 2015. <https://doi.org/10.1177/0363546514566192>.
6. Roberts, T. P. L., and E. S. Schwartz. Principles and implementation of diffusion-weighted and diffusion tensor imaging. *Pediatr. Radiol.* 37(8):739–748, 2007. <https://doi.org/10.1007/s00247-007-0516-z>.
7. Le Bihan, D., and H. Johansen-Berg. Diffusion MRI at 25: Exploring brain tissue structure and function. *Neuroimage.* 61(2):324–341, 2012. <https://doi.org/10.1016/j.neuroimage.2011.11.006>.
8. Hooijmans, M. T., B. M. Damon, M. Froeling, M. J. Versluis, J. Burakiewicz, J. J. G. M. Verschuuren, E. H. Niks, A. G. Webb, and H. E. Kan. Evaluation of skeletal muscle DTI in patients with duchenne muscular dystrophy: skeletal muscle DTI in DMD.

- NMR Biomed.* 28(11):1589–1597, 2015. <https://doi.org/10.1002/nbm.3427>.
9. Damon, B. M., M. Froeling, A. K. W. Buck, J. Oudeman, Z. Ding, A. J. Nederveen, E. C. Bush, and G. J. Strijkers. Skeletal muscle diffusion tensor-MRI fiber tracking: rationale, data acquisition and analysis methods, applications and future directions: skeletal muscle DT-MRI fiber tracking. *NMR Biomed.* 30(3):e3563, 2017. <https://doi.org/10.1002/nbm.3563>.
 10. Naughton, N. M., and J. G. Georgiadis. Global sensitivity analysis of skeletal muscle dMRI metrics: effects of microstructural and pulse parameters. *Magn. Reson. Med.* 83(4):1458–1470, 2020. <https://doi.org/10.1002/mrm.28014>.
 11. Kakkad, S., J. Zhang, A. Akhbardeh, D. Jacob, B. Krishnamachary, M. Solaiyappan, M. A. Jacobs, V. Raman, D. Leibfritz, K. Glunde, and Z. M. Bhujwalla. Collagen fibers mediate MRI-detected water diffusion and anisotropy in breast cancers. *Neoplasia (United States)*. 18(10):585–593, 2016. <https://doi.org/10.1016/j.neo.2016.08.004>.
 12. Meder, R., S. K. de Visser, J. C. Bowden, T. Bostrom, and J. M. Pope. Diffusion tensor imaging of articular cartilage as a measure of tissue microstructure. *Osteoarthritis Cartilage*. 14(9):875–881, 2006. <https://doi.org/10.1016/j.joca.2006.03.002>.
 13. Raya, J. G., G. Melkus, S. Adam-Neumair, O. Dietrich, E. Mützel, B. Kahr, M. F. Reiser, P. M. Jakob, R. Putz, and C. Glaser. Change of diffusion tensor imaging parameters in articular cartilage with progressive proteoglycan extraction. *Invest. Radiol.* 46(6):401–409, 2011. <https://doi.org/10.1097/RLI.0b013e3182145aa8>.
 14. Ghazanfari, S., A. Driessen-Mol, G. J. Strijkers, F. M. Kanters, F. P. Baaijens, and C. V. Bouten. A comparative analysis of the collagen architecture in the carotid artery: second harmonic generation versus diffusion tensor imaging. *Biochem. Biophys. Res. Commun.* 426(1):54–58, 2012. <https://doi.org/10.1016/j.bbrc.2012.08.031>.
 15. Ghazanfari, S., A. Driessen-Mol, G. J. Strijkers, F. P. T. Baaijens, and C. V. C. Bouten. The evolution of collagen fiber orientation in engineered cardiovascular tissues visualized by diffusion tensor imaging. *PLoS ONE*. 10(5):e0127847, 2015. <https://doi.org/10.1371/journal.pone.0127847>.
 16. Qi, W., P. Zhao, Z. Sun, X. Ma, H. Wang, W. Wu, Z. Wen, Z. Kisrieva-Ware, P. K. Woodard, Q. Wang, R. C. McKinstry, A. G. Cahill, and Y. Wang. Magnetic resonance diffusion tensor imaging of cervical microstructure in normal early and late pregnancy in vivo. *Am. J. Obstet. Gynecol.* 224(1):101.e1–101.e11, 2021. <https://doi.org/10.1016/j.ajog.2020.07.014>.
 17. Ferizi, U., I. Rossi, Y. Lee, M. Lendhey, J. Teplensky, O. D. Kennedy, T. Kirsch, J. Bendardino, and J. G. Raya. Diffusion tensor imaging of articular cartilage at 3T correlates with histology and biomechanics in a mechanical injury model. *Magn. Reson. Med.* 78(1):69–78, 2017. <https://doi.org/10.1002/mrm.26336>.
 18. Yang, X., M. Li, D. Chen, D. Shi, Z. Zhou, B. Zhu, and Q. Jiang. Diffusion tensor imaging for anatomical and quantitative evaluation of the anterior cruciate ligament and ACL grafts: a preliminary study. *J. Comput. Assist. Tomogr.* 38(4):489–494, 2014. <https://doi.org/10.1097/RCT.0000000000000078>.
 19. Yang, X., D. Chen, M. Li, D. Shi, B. Zhu, and Q. Jiang. Diffusion tensor imaging of the anterior cruciate ligament graft after reconstruction: repeatability and diffusion tensor imaging metrics. *J. Comput. Assist. Tomogr.* 39(2):244–249, 2015. <https://doi.org/10.1097/RCT.0000000000000198>.
 20. Van Dyck, P., M. Froeling, E. De Smet, P. Pullens, M. Torfs, P. Verdonk, J. Sijbers, P. M. Parizel, and B. Jeurissen. Diffusion tensor imaging of the anterior cruciate ligament graft. *J. Magn. Reson. Imaging*. 46(5):1423–1432, 2017. <https://doi.org/10.1002/jmri.25666>.
 21. Van Dyck, P., T. Billiet, D. Desbuquoit, P. Verdonk, C. H. Heusdens, E. Roelant, J. Sijbers, and M. Froeling. Diffusion tensor imaging of the anterior cruciate ligament graft following reconstruction: a longitudinal study. *European Radiology*. <https://doi.org/10.1007/s00330-020-07051-w>.
 22. Van Dyck, P., M. Froeling, C. H. Heusdens, J. Sijbers, A. Ribbens, and T. Billiet. Diffusion tensor imaging of the anterior cruciate ligament following primary repair with internal bracing: a longitudinal study. *J. Orthop. Res.* 2020:1–13, 2019. <https://doi.org/10.1002/jor.24684>.
 23. Liu, S., J. Liu, W. Chen, L. Zhang, S. Wu, F. Wang, J. Pan, M. Luo, X. Liu, and S. Zhang. Diffusion tensor imaging for quantitative assessment of anterior cruciate ligament injury grades and graft. *J. Magn. Reson. Imaging*. 52(5):1475–1484, 2020. <https://doi.org/10.1002/jmri.27322>.
 24. Sarman, H., H. Atmaca, O. Cakir, U. S. Muezzinoglu, Y. Anik, K. Memisoglu, T. Baran, and C. Isik. Assessment of postoperative tendon quality in patients with achilles tendon rupture using diffusion tensor imaging and tendon fiber tracking. *J. Foot Ankle Surg.* 54(5):782–786, 2015. <https://doi.org/10.1053/j.jfas.2014.12.025>.
 25. K. Wengler, D. Tank, T. Fukuda, J. M. Paci, M. Huang, M. E. Schweitzer and X. He, Diffusion tensor imaging of human Achilles tendon by stimulated echo readout-segmented EPI (ste-RS-EPI): Wengler et al., *Magnetic Resonance in Medicine* 80(6):2464–2474, 2018. <https://doi.org/10.1002/mrm.27220>.
 26. Wengler, K., T. Fukuda, D. Tank, D. E. Komatsu, M. Paulus, M. Huang, E. S. Gould, M. E. Schweitzer, and X. He. In vivo evaluation of human patellar tendon microstructure and microcirculation with diffusion MRI. *J. Magn. Reson. Imaging*. 51(3):780–790, 2020. <https://doi.org/10.1002/jmri.26898>.
 27. Zellers, J. A., M. Edalati, J. D. Eekhoff, R. McNish, S. Y. Tang, S. P. Lake, M. J. Mueller, M. K. Hastings, and J. Zheng. Quantitative MRI predicts tendon mechanical behavior, collagen composition, and organization. *J. Orthopaed. Res.*, 2022, <https://doi.org/10.1002/jor.25471>
 28. Skelley, N. W., R. M. Castile, P. C. Cannon, C. I. Weber, R. H. Brophy, and S. P. Lake. Regional variation in the mechanical and microstructural properties of the human anterior cruciate ligament. *Am. J. Sports Med.* 44(11):2892–2899, 2016. <https://doi.org/10.1177/0363546516654480>.
 29. Tornifoglio, B., A. J. Stone, R. D. Johnston, S. S. Shahid, C. Kerskens, and C. Lally. Diffusion tensor imaging and arterial tissue: establishing the influence of arterial tissue microstructure on fractional anisotropy, mean diffusivity and tractography. *Sci. Rep.* 10(1):1–12, 2020. <https://doi.org/10.1038/s41598-020-77675-x>.
 30. Fieremans, E., and H. H. Lee. Physical and numerical phantoms for the validation of brain microstructural MRI: a cookbook. *Neuroimage*. 182(June):39–61, 2018. <https://doi.org/10.1016/j.neuroimage.2018.06.046>.
 31. Fieremans, E., Y. De Deene, S. Delputte, M. S. Özdemir, E. Achten, and I. Lemahieu. The design of anisotropic diffusion phantoms for the validation of diffusion weighted magnetic resonance imaging. *Phys. Med. Biol.* 53(19):5405–5419, 2008. <https://doi.org/10.1088/0031-9155/53/19/009>.
 32. Fieremans, E., Y. De Deene, S. Delputte, M. S. Özdemir, Y. D’Asseler, J. Vlassenbroeck, K. Deblaere, E. Achten, and I. Lemahieu. Simulation and experimental verification of the diffusion in an anisotropic fiber phantom. *J. Magn. Reson.* 190(2):189–199, 2008. <https://doi.org/10.1016/j.jmr.2007.10.014>.
 33. Poupon, C., B. Rieul, I. Kezele, M. Perrin, F. Poupon, and J.-F. Mangin. New diffusion phantoms dedicated to the study and validation of high-angular-resolution diffusion imaging (HARDI) models: HARDI validation phantoms. *Magn. Reson. Med.* 60(6):1276–1283, 2008. <https://doi.org/10.1002/mrm.21789>.
 34. Pullens, P., A. Roebroek, and R. Goebel. Ground truth hardware phantoms for validation of diffusion-weighted MRI applications.

- J. Magn. Reson. Imaging.* 32(2):482–488, 2010. <https://doi.org/10.1002/jmri.22243>.
35. Tourell, M. C., S. K. Powell, and K. I. Momot. Diffusion tensor of water in partially aligned fibre networks. *J. Phys. D Appl. Phys.* <https://doi.org/10.1088/0022-3727/46/45/455401>.
 36. Lee, W., H. Rahman, M. E. Kersh, and K. C. Toussaint. Application of quantitative second-harmonic generation microscopy to posterior cruciate ligament for crimp analysis studies. *J. Biomed. Opt.* 22(4):046009, 2017. <https://doi.org/10.1117/1.jbo.22.4.046009>.
 37. Thorpe, C. T., C. Klemt, G. P. Riley, H. L. Birch, P. D. Clegg, and H. R. Screen. Helical sub-structures in energy-storing tendons provide a possible mechanism for efficient energy storage and return. *Acta Biomater.* 9(8):7948–7956, 2013. <https://doi.org/10.1016/j.actbio.2013.05.004>.
 38. Peterson, B. E., and S. E. Szczesny. Dependence of tendon multiscale mechanics on sample gauge length is consistent with discontinuous collagen fibrils. *Acta Biomater.* 117:302–309, 2020. <https://doi.org/10.1016/j.actbio.2020.09.046>.
 39. Szczesny, S. E., and D. M. Elliott. Interfibrillar shear stress is the loading mechanism of collagen fibrils in tendon. *Acta Biomater.* 10(6):2582–2590, 2014. <https://doi.org/10.1016/j.actbio.2014.01.032>.
 40. Hearle, J. W., P. Grosberg, and S. Backer. Structural Mechanics of Fibers, Yarns, and Fabrics. New York: Wiley-Interscience, 1969.
 41. Reese, S. P., S. A. Maas, and J. A. Weiss. Micromechanical models of helical superstructures in ligament and tendon fibers predict large Poisson's ratios. *J. Biomech.* 43(7):1394–1400, 2010. <https://doi.org/10.1016/j.jbiomech.2010.01.004>.
 42. Le, C. V., and D. G. Phillips. The low-stress tensile behaviour of single worsted yarns. *J. Text. Inst.* 98(5):421–429, 2007. <https://doi.org/10.1080/00405000701570856>.
 43. Pineda Guzman, R. A., and M. E. Kersh. Replication of the tensile behavior of knee ligaments using architected acrylic yarn. *J. Mech. Behav. Biomed. Mater.* 118:104339, 2021. <https://doi.org/10.1016/j.jmbbm.2021.104339>.
 44. Arant, L. R., and J. D. Roth. Development and evaluation of ligament phantoms targeted for shear wave tensiometry. *J. Mech. Behav. Biomed. Mater.* 126:104984, 2021. <https://doi.org/10.1016/j.jmbbm.2021.104984>.
 45. Handsfield, G. G., L. C. Slane, and H. R. Screen. Nomenclature of the tendon hierarchy: an overview of inconsistent terminology and a proposed size-based naming scheme with terminology for multi-muscle tendons. *J. Biomech.* 49(13):3122–3124, 2016. <https://doi.org/10.1016/j.jbiomech.2016.06.028>.
 46. Naughton, N. M., C. G. Tennyson, and J. G. Georgiadis. Lattice Boltzmann method for simulation of diffusion magnetic resonance imaging physics in multiphase tissue models. *Phys. Rev. E.* 102(4):043305, 2020. <https://doi.org/10.1103/PhysRevE.102.043305>.
 47. Veraart, J., E. Fieremans, and D. S. Novikov. Diffusion MRI noise mapping using random matrix theory: diffusion MRI noise mapping. *Magn. Reson. Med.* 76(5):1582–1593, 2016. <https://doi.org/10.1002/mrm.26059>.
 48. Tournier, J.-D., R. Smith, D. Raffelt, R. Tabbara, T. Dhollander, M. Pietsch, D. Christiaens, B. Jeurissen, C.-H. Yeh, and A. Connelly. MRtrix3: a fast, flexible and open software framework for medical image processing and visualisation. *Neuroimage.* 202:116137, 2019. <https://doi.org/10.1016/j.neuroimage.2019.116137>.
 49. Koay, C. G., and P. J. Basser. Analytically exact correction scheme for signal extraction from noisy magnitude mr signals. *J. Magn. Reson.* 179(2):317–322, 2006.
 50. Anderson, A. W. Theoretical analysis of the effects of noise on diffusion tensor imaging. *Magn. Reson. Med.* 46(6):1174–1188, 2001.
 51. Damon, B. M. Effects of image noise in muscle diffusion tensor (dt)-mri assessed using numerical simulations. *Magn. Reson. Med.* 60(4):934–944, 2008.
 52. Damon, B. M., Z. Ding, M. T. Hooijmans, A. W. Anderson, X. Zhou, C. L. Coolbaugh, M. K. George, and B. A. Landman. A MATLAB toolbox for muscle diffusion-tensor MRI tractography. *J. Biomech.* 124:110540, 2021. <https://doi.org/10.1016/j.jbiomech.2021.110540>.
 53. P. Fratzl, Collagen: structure and mechanics, an introduction. In: Collagen, edited by P. Fratzl. Boston: Springer, 2008, pp. 1–13. https://doi.org/10.1007/978-0-387-73906-9_1
 54. Thornton, G. M., T. D. Schwab, and T. R. Oxland. Cyclic loading causes faster rupture and strain rate than static loading in medial collateral ligament at high stress. *Clin. Biomech.* 22(8):932–940, 2007. <https://doi.org/10.1016/j.clinbiomech.2007.05.004>.
 55. van Wyk, C. M. 20—Note on the compressibility of wool. *J. Text. Inst. Trans.* 37(12):T285–T292, 1946. <https://doi.org/10.1080/19447024608659279>.
 56. Lynch, H. A., W. Johannessen, J. P. Wu, A. Jawa, and D. M. Elliott. Effect of fiber orientation and strain rate on the nonlinear uniaxial tensile material properties of tendon. *J. Biomech. Eng.* 125(5):726–731, 2003. <https://doi.org/10.1115/1.1614819>.
 57. Lorenz, R., M. E. Bellemann, J. Hennig, and K. A. Il'Yasov. Anisotropic phantoms for quantitative diffusion tensor imaging and fiber-tracking validation. *Appl. Magn. Reson.* 33(4):419–429, 2008. <https://doi.org/10.1007/s00723-008-0087-7>.
 58. Fung, D. T., V. M. Wang, D. M. Laudier, J. H. Shine, J. Basta-Pljakic, K. J. Jepsen, M. B. Schaffler, and E. L. Flatow. Subrupture tendon fatigue damage. *J. Orthop. Res.* 27(2):264–273, 2009. <https://doi.org/10.1002/jor.20722>.
 59. Freedman, B. R., A. Zuskov, J. J. Sarver, M. R. Buckley, and L. J. Soslowky. Evaluating changes in tendon crimp with fatigue loading as an ex vivo structural assessment of tendon damage. *J. Orthop. Res.* 33(6):904–910, 2015. <https://doi.org/10.1002/jor.22875>.
 60. Alia, A., G. Fantozzi, N. Godin, J. Adrien, H. Osmani, and P. Reynaud. Multi-instrumented analysis of fatigue behavior and damage mechanisms in jute fiber-reinforced polyester composites. *Int. J. Fatigue.* 167:107306, 2023. <https://doi.org/10.1016/j.ijfatigue.2022.107306>.
 61. Imhauser, C. W., R. N. Kent, J. Boorman-Padgett, R. Thein, T. L. Wickiewicz, and A. D. Pearle. New parameters describing how knee ligaments carry force in situ predict interspecimen variations in laxity during simulated clinical exams. *J. Biomech.* 64:212–218, 2017. <https://doi.org/10.1016/j.jbiomech.2017.09.032>.
 62. Screen, H. R. C., D. A. Lee, D. L. Bader, and J. C. Shelton. An investigation into the effects of the hierarchical structure of tendon fascicles on micromechanical properties. *Proc. Inst. Mech. Eng. Part H J. Eng. Med.* 218:109–119, 2004.
 63. Woo, S. L.-Y. Biomechanics of tendons and ligaments. *Front. Biomech.* 180–195, 1986. https://doi.org/10.1007/978-1-4612-4866-8_14.
 64. Zitnay, J. L., G. S. Jung, A. H. Lin, Z. Qin, Y. Li, S. M. Yu, M. J. Buehler, and J. A. Weiss. Accumulation of collagen molecular unfolding is the mechanism of cyclic fatigue damage and failure in collagenous tissues. *Sci. Adv.* <https://doi.org/10.1126/sciadv.aba2795>.
 65. Firminger, C. R., and W. B. Edwards. Effects of cyclic loading on the mechanical properties and failure of human patellar tendon. *J. Biomech.* 120:110345, 2021.
 66. Wojtys, E. M., M. L. Beaulieu, and J. A. Ashton-Miller. New perspectives on ACL injury: on the role of repetitive sub-maximal knee loading in causing ACL fatigue failure. *J. Orthop. Res.* 34(12):2059–2068, 2016. <https://doi.org/10.1002/jor.23441>.

Publisher's Note Springer Nature remains neutral with regard to jurisdictional claims in published maps and institutional affiliations.

Springer Nature or its licensor (e.g. a society or other partner) holds exclusive rights to this article under a publishing agreement with the

author(s) or other rightsholder(s); author self-archiving of the accepted manuscript version of this article is solely governed by the terms of such publishing agreement and applicable law.